
On the Practicality of Deterministic Epistemic Uncertainty

Janis Postels^{*1}, Mattia Segu^{*1 2}, Tao Sun¹, Luc Van Gool¹, Fisher Yu¹ Federico Tombari^{3 4}
¹ ETH Zurich ² Max Planck ETH CLS ³ Google ⁴ TUM Munich
{jpostels, segum, taosun47, vangool}@ethz.ch, i@yf.io tombari@google.com

Abstract

A set of novel approaches for estimating epistemic uncertainty in deep neural networks with a single forward pass has recently emerged as a valid alternative to Bayesian Neural Networks. On the premise of informative representations, these deterministic uncertainty methods (DUMs) achieve strong performance on detecting out-of-distribution (OOD) data while adding negligible computational costs at inference time. However, it remains unclear whether DUMs are well calibrated and can seamlessly scale to real-world applications - both prerequisites for their practical deployment. To this end, we first provide a taxonomy of DUMs, evaluate their calibration under continuous distributional shifts and their performance on OOD detection for image classification tasks. Then, we extend the most promising approaches to semantic segmentation. We find that, while DUMs scale to realistic vision tasks and perform well on OOD detection, the practicality of current methods is undermined by poor calibration under realistic distributional shifts.

1 Introduction

Despite the dramatic enhancement of predictive performance by deep learning (DL), its adoption remains limited due to unpredictable failure on out-of-distribution (OOD) samples [1, 2] and adversarial attacks [3]. Uncertainty estimation techniques aim at bridging this gap by providing accurate confidence levels on a model’s output, allowing for a safe deployment of neural networks (NNs) in life-critical tasks, *e.g.* autonomous driving or medical applications.

2 Related Work

Sources of Uncertainty. Uncertainty in a model’s predictions can arise from two different sources [4, 5]. While *aleatoric* uncertainty encompasses the noise inherent in the data and is consequently irreducible [4], *epistemic* uncertainty quantifies the uncertainty associated with choosing the model parameters based on limited information, and vanishes - in principle - in the limit of infinite data. This work distinguishes two properties of epistemic uncertainty - its performance on detecting OOD samples and its calibration (*i.e.* its correlation with model performance under distributional shifts). While the latter has been explored in the case of probabilistic approaches to uncertainty estimation [6], to the best of our knowledge, we are the first to investigate the behaviour of Deterministic Uncertainty Methods (DUMs) in this scenario. Notably, [7] evaluates prominent scalable epistemic uncertainty estimates on semantic segmentation. However, they investigate calibration only on in-distribution data.

Bayesian Neural Networks (BNNs) [8, 9] represent a principled way of measuring uncertainty. However, the intractability of their posterior distribution requires approximate inference methods, such as Markov Chain Monte-Carlo [8] or Variational Inference (VI) [10]. While these methods

*The first two authors contributed equally.

traditionally struggle with large datasets and architectures, a variety of scalable approaches - often based on VI - has recently emerged.

Deep Ensembles, which typically consist of identical models trained from different initializations, have been introduced to the deep learning community by Lakshminarayanan *et al.* [11] and extended by [12, 13]. While deep ensembles are widely regarded as a strong baseline for estimating epistemic uncertainty, they come with a high computational costs as well as their memory footprint.

Efficient Approaches. Recently, a variety of approaches based on stochastic regularization have been developed [14, 15, 16, 17]. By keeping stochasticity switched on at inference time, they estimate uncertainty using multiple forward passes. Moreover, efficient ensemble methods were proposed producing predictions using a single model [12, 13, 18]. Despite these methods show promising results on large-scale tasks while being parameter-efficient, they still need multiple forward passes through the model, which can render them impractical given a limited computational budget. To enable uncertainty modelling in real-time and resource-demanding tasks, recent work has focused on providing uncertainty estimates with a *single forward pass*. For instance, one line of work proposes a principled approach for variance propagation in NNs [19, 20, 21].

Recently, a new family of methods - DUMs - showed promising results in uncertainty estimation for OOD detection. By leveraging distances and densities in the feature space of a NN, these methods provide confidence estimates while adding negligible computational cost. Since they are united in their deterministic treatment of the weights, we term them Deterministic Uncertainty Methods (DUMs). The next section provides a taxonomy of DUMs, summarizing these recently emerging approaches to quantifying epistemic uncertainty.

3 Taxonomy for Deterministic Uncertainty Quantification

DUMs		Uncertainty Estimation Method			
		Discriminative		Generative	
		Distance from class centroid	Gaussian Processes	Gaussian Mixture Models	Normalizing Flows
Target Property	Distance awareness	DCS [22], DUQ [23]	SNGP [24], DUE [25]	DDU [26]	-
	Informative representations	-	-	DCU [27], MIR [28]	Invertible networks [29, 30, 31]

Table 1: Taxonomy of DUMs. Methods are grouped according to the target property of the hidden representations (rows), and their uncertainty estimation method (columns).

This section proposes a taxonomy of existing DUMs. To quantify epistemic uncertainty deterministically, the distribution of the hidden representations of a neural network needs to represent the input distribution. However, discriminative models suffer from the fundamental problem of feature collapse. Thus, we firstly categorize DUMs according to the regularization method used to counteract feature collapse (Sec. 3.1). Moreover, we cluster DUMs according to the method used for uncertainty estimation (Sec. 3.2). Tab. 1 shows an overview of the resulting taxonomy.

Feature Collapse. Discriminative models can learn to discard large part of their input information, as exploiting spurious correlations may lead to better performance on the training data distribution [32, 33]. The invariant representations learned by discriminative models extend to OOD data, resulting in a collapse of OOD embeddings to in-distribution features in the hidden space. This problem is known as *feature collapse* [23], and it makes OOD detection based on high-level representations impossible.

3.1 Regularization of Hidden Representations

We group DUMs according to how feature collapse is tackled, enabling OOD detection based on latent representations. In particular, we identify two main paradigms - distance awareness and informative representations - which we discuss in Sec. 3.1.1 and Sec. 3.1.2.

3.1.1 Distance Awareness

The fundamental idea of distance-aware hidden representations is to avoid feature collapse by enforcing distances between latent representations to mirror distances in the input space. This can be achieved by constraining the Lipschitz constant, as it enforces a lower and an upper bound to expansion and contraction performed by an underlying neural network. A lower bound is associated with *sensitivity*, since it enforces that different inputs are mapped to distinct latent representations and, thus, provides a solution to feature collapse. Moreover, an upper bound enforces *smoothness* of the hidden representations, *i.e.* small changes in the input do not result in large changes in the latent space. More formally, given any pair of inputs x_1 and x_2 the following lower and upper bounds must hold for the resulting activation of a feature extractor f_θ with parameters θ : $c_1 \|x_1 - x_2\|_I \leq \|f_\theta(x_1) - f_\theta(x_2)\|_F \leq c_2 \|x_1 - x_2\|_I$. c_1 and c_2 denote respectively the lower and upper bound for the Lipschitz constant, and $\|\cdot\|_I$ and $\|\cdot\|_F$ are the chosen metrics in the input and feature space respectively. While there exist other approaches, *e.g.* [34], recent proposals have primarily adopted two methods to impose the bi-Lipschitz constraint.

Gradient Penalty. First introduced to regularize the Lipschitz constant in GAN training [35], a two-sided gradient penalty is used as an additional loss term to enforce detectability in the feature space of changes in the input by DUQ [23]. The gradient penalty is formulated as an additional loss term that regularises the Frobenius norm $\|J\|_F$ of the Jacobian J of a NN to enforce a bi-Lipschitz constraint. Therefore, the training loss of a NN is typically enhanced with the absolute difference between $\|J\|_F$ and some chosen positive constant (see supplement or [23] for more details).

Spectral Normalization. The two-sided gradient penalty described above requires backpropagating through the Jacobian of a NN and is, thus, computationally demanding. A more efficient technique is Spectral Normalization (SN) [36]. For each layer, SN normalizes the weights W of each layer using their spectral norm $sn(W)$ to constrain the bi-Lipschitz constant. Thus, weight matrices are normalized according to: $W_{sn} = \frac{W}{c \cdot sn(W)}$. Note, that this soft constraint becomes hard for $c = 1$. We refer to the supplement or [24] for further details. Various DUMs - SNGP [24], DUE [25] and DDU [26] - rely on SN of the weight matrices to enforce distance-awareness of hidden representations.

Note that the Lipschitz constraint is defined with respect to a predefined distance measure, which can be difficult to choose for many high-dimensional data distributions of practical interest. A popular choice, also adopted by [23, 24, 25], is the L_2 distance. Moreover, principled approaches to provide exact singular values in convolutional layers [37] result in prohibitive computational complexity; the spectral normalization approximations typically adopted by the methods previously described have been found to be sub-optimal *et al.* [38], and its interaction with losses, architecture and optimization is yet to be fully understood [39]. Consequently, Lipschitz regularization with respect to a potentially meaningless distance measure may result in overly sensitive models. Sec. 4.1.1 analyses the impact of regularization strength on OOD detection.

3.1.2 Informative Representations

While methods enforcing distance-awareness achieve remarkable performance in OOD detection, they do not explicitly preserve sample-specific information. Consequently, depending on the underlying distance metric they may discard useful information about the input or act overly sensitive. An alternative line of work proposes to avoid feature collapse by learning informative representations [27, 28, 29, 30, 31, 40], thus forcing discriminative models to preserve information beyond what required by its target task in its hidden representations independent of the choice of an underlying distance metric. Notably, while representations that are aware of distances in the input space are arguably also informative, both categories remain fundamentally different in their approach to feature collapse. While distance-awareness is based on the choice of a specific distance metric tying together input and latent space, informative representations incentivize the network to store more information about the input using an auxiliary task [27, 28] or forbid information loss by construction [29, 30, 31]. We identify three distinct families of approaches to enforce informative representations.

Contrastive learning [27, 41] has emerged as an approach for learning representations that are both informative and discriminative. This is utilized by Wu *et al.* [27], who build on top of SimCLR [42] to regularize hidden representations for a discriminative task by using an auxiliary contrastive loss to force representations to further discriminate between individual instances.

Reconstruction regularization [28] instead forces the intermediate activations to embody a complete representation of the input space. This is achieved by adding a decoder branch fed with the activations of a given layer to reconstruct the input. Since this method aims at producing Maximally Informative Representations, we term it MIR.

Invertible Neural Networkss (INNs) [29, 30, 31, 43], built via a cascade of homeomorphic layers, cannot discard information except at the final classification stage. Consequently, the mutual information between input and hidden representation is retained by construction. Interestingly, Behrmann *et al.* [44] showed that a ResNet is invertible if its Lipschitz constant is lower than 1, meaning that invertible ResNets both possess highly-informative representations and satisfy distance-awareness. However, note that this is not a necessary condition for invertibility, and thus information preservation, in general.

3.2 Uncertainty Estimation

We now describe the different approaches to quantifying uncertainty based on such regularized representations. We distinguish two directions - generative and discriminative approaches. While generative approaches use the likelihood produced by an explicit generative model of the distribution of hidden representations as a proxy for uncertainty, discriminative methods directly use the predictions based on regularized representations to quantify uncertainty.

Generative approaches estimate the distribution of hidden representations post-training and use the likelihood as uncertainty metric to detect OOD samples. Wu *et al.* [27] propose a Deep Contrastive Uncertainty (DCU) method to train an additional deep network from the representation space to a distribution space, where the variance of the distribution is used as a confidence measure. MIR [28] and DDU [26] fit a class-conditional GMM to their regularized hidden representations and use the log-likelihood as an epistemic uncertainty proxy. A special instance of the generative approaches are INNs as they directly estimate the training data distribution. This allows using the likelihood of the input data as a proxy of uncertainty. While this idea is appealing, it can lead to training difficulties, imposes strong constraints on the underlying feature extractor and in some instances even remains susceptible to OOD data [45].

Discriminative approaches use the predictions based on regularized representations to directly assess confidence. Mandelbaum *et al.* [22] propose to use a Distance-based Confidence Score (DCS) to estimate local density at a point as the Euclidean distance in the embedded space between the point and its k nearest neighbors in the training set. Similarly, DUQ [23] builds on Radial Basis Function (RBF) networks [46] and propose a novel centroid updating scheme. Uncertainty is estimated as the distance between the model output and the closest centroid. DUMs adopting SN [24, 25], and thus preserving L_2 distances, typically fit Gaussian processes (GPs) with RBF kernels on top of the learned feature space, extending distance awareness to the output layer. In particular, SNGP [24] relies on a Laplace approximation of the GP based on the random Fourier feature (RFF) expansion of the GP posterior [47]. DUE [25] leverages instead the inducing point approximation [48, 49], allowing to pick an arbitrarily large number of inducing points without overfitting [50]. The uncertainty is then derived respectively as the Dempster-Shafer metric [24] or the softmax entropy [25].

4 Evaluation of Deterministic Epistemic Uncertainty

We first benchmark DUMs on popular image classification datasets (Sec. 4.1). Further, we evaluate how such techniques scale to harder tasks, *e.g.* semantic segmentation, by extending the most promising DUMs to dense prediction tasks (Sec. 4.2). Finally, in Sec. 4.2.3 we find that uncertainty from the current generation of DUMs is considerably worse calibrated under realistic distributional shift than scalable approaches based on stochastic regularization, *i.e.* MC dropout.

Baselines. We compare DUMs with two established baselines for estimating epistemic uncertainty on image classification (Sec. 4.1) - Monte-Carlo (MC) dropout [15] and deep ensembles [11]. On semantic segmentation (Sec. 4.2) we compare only against MC dropout since maintaining several set of weights of a large NN dramatically increases memory requirements. Note, that while these baselines are expected to predict reasonable uncertainty, their computational footprint greatly outweighs DUMs. We also report the performance of the softmax entropy as a baseline deterministic uncertainty method.

Methods. For this comparison, we choose DUMs according to their potential to benefit real-world applications. We thus value DUMs that can readily scale to large vision tasks (*e.g.* semantic segmentation). Therefore, we exclude DUMs that regularize hidden representations using contrastive learning [27], which requires very large batch sizes and long training times, and invertible neural networks [30, 31], which enforce strict constraints on the underlying architecture (*e.g.* fixed dimensionality of hidden representations) and often lead to training instabilities. Moreover, we do not include DCS [22] since it only leads to a marginal improvement over the softmax entropy according to their own experiments, and since their contrastive loss only operates on class centroids and, thus, is not expected to lead to distance awareness within clusters.

OOD detection metrics. We follow prior work [24, 28] and compute Area Under the Receiver Operating Characteristic (AUROC) and Area Under the Precision-Recall curve (AUPR) between test data that originates from the same distribution as the training data and data originating from another dataset (Sec. 4.1.1).

Calibration metric. In order to assess the calibration of uncertainty estimates under distributional shifts, we need to introduce a novel metric, since Expected Calibration Error (ECE) [51] and Brier score [52] are limited to probabilistic forecasts (*i.e.* methods producing calibrated probabilities). Therefore, we calculate the Area Under the Lift Curve (AULC) [53], which we obtain by ordering the predictions according to increasing uncertainty and plotting the performance (*e.g.* accuracy) of all samples with an uncertainty estimate smaller than a certain quantile of the uncertainty against the quantile of uncertainty. Formally, given a set of uncertainty quantiles $q_i \in [0, 1]$, $i \in [1, \dots, N]$, with some quantile step width $0 < s < 1$ and the function $F(q_i)$ which returns the accuracy of all samples with uncertainty $u < q_i$, we define the AULC as $AULC = -1 + \sum_{i \in [1, \dots, N]} s \frac{F(q_i)}{F_R(q_i)}$. Here, $F_R(\cdot)$ refers to a baseline uncertainty estimate that corresponds to random guessing, and we subtract 1 to shift the performance of the random baseline to zero. Note, if an uncertainty estimate is anti-correlated with a models’ performance, this score can also be negative. To alleviate bias towards better performing models, we further compute the Relative Area Under the Lift Curve (rAULC) by dividing the AULC by the AULC of a hypothetical (optimal) uncertainty estimation that perfectly orders samples according to model performance. In classification samples are ordered according to correct/incorrect prediction. In semantic segmentation we use the image-level pixel accuracy.

4.1 Image Classification

Datasets. We train DUMs on MNIST [54], FashionMNIST [55]), CIFAR-10 [56] and SVHN [57]). Further, when evaluating OOD detection, we also evaluate on Omniglot [58] for models trained on MNIST/FashionMNIST and on STL-10 [59] for models trained on CIFAR10/SVHN.

Models and optimization. For the experiments on MNIST and Fashion-MNIST, we employ a multilayer perceptron (MLP) as feature extractor with 3 hidden layers of 100 dimensions each and ReLU activation functions. When training on CIFAR-10 and SVHN, we use a ResNet-18 [60] as backbone. Each DUM is associated with a particular hyperparameter for the regularization of its hidden representations. We choose the hyperparameter such that it minimizes the validation loss in the experiments on OOD detection and calibration. However, this section also includes an analysis of the sensitivity of calibration and OOD detection performance to the hyperparameter (Fig. 2). All results are averages 5 distinct trainings. We refer to the supplement for a detailed description on the optimization procedure for each DUM.

Continuous distributional shifts. We evaluate calibration of DUMs on continuously shifted test data. Therefore, we apply rotations to MNIST/FashionMNIST in steps of 20° from 0° to 180° . When evaluating on SVHN/CIFAR10 we add Gaussian noise of increasing standard deviation σ to the test data. We vary σ in steps of 0.05 from 0 to 0.25 (on normalized data).

4.1.1 Results

Calibration under continuous distributional shift. Tab. 2 shows accuracy on the test set and calibration performance in terms of rAULC. With the exception of DUQ, which we find to be prone to training instabilities, all DUMs achieve similar predictive performance as MC dropout, deep ensembles and standard softmax models. In terms of uncertainty calibration, we observe that in particular DUE, SNGP and MIR compete with established uncertainty estimation methods (*e.g.* MC dropout) across most datasets and both types of distributional shifts. Consequently, these approaches

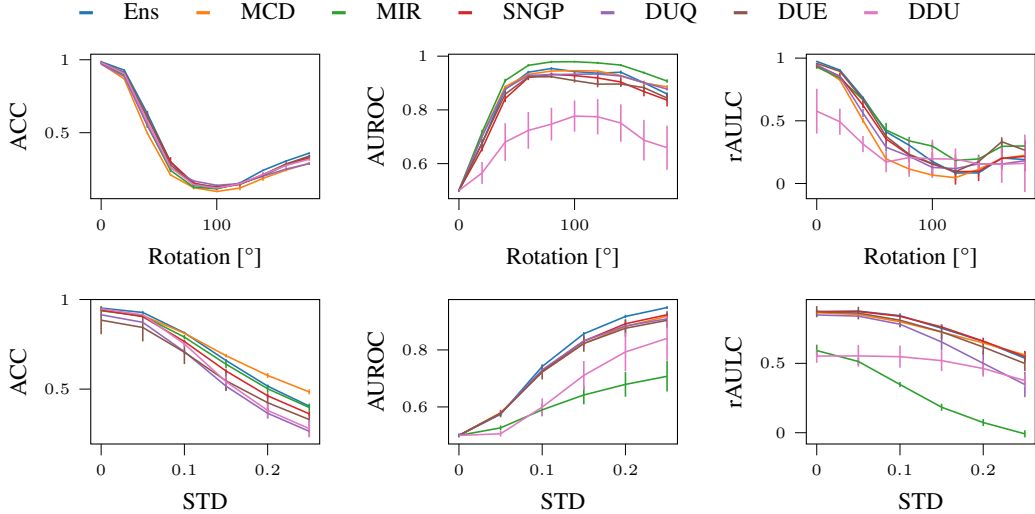


Figure 1: We compare DUMs and the baselines (MC dropout (MCD), ensembles (Ens)) under continuous distributional shifts. Therefore, we plot accuracy (LEFT), AUROC (CENTER) and rAULC (RIGHT) against the perturbation magnitude for a MLP trained on MNIST (TOP) and a ResNet-18 on SVHN (BOTTOM). We perturb MNIST using rotations and SVHN using additive Gaussian noise. The AUROC is computed against unperturbed test data. Most DUMs demonstrate similar behaviour as the baselines, except DDU. While MIR shows strong performance on MNIST, its performance drops on CIFAR10.

Method	MNIST		FashionMNIST		CIFAR10		SVHN	
	Acc	rAULC	Acc	rAULC	Acc	rAULC	Acc	rAULC
Softmax	98.1 ± 0.1	54.1 ± 3.4	88.1 ± 0.2	7.1 ± 2.9	84.5 ± 0.2	43.4 ± 17.4	93.2 ± 0.2	84.2 ± 0.5
Dropout	97.2 ± 0.1	59.2 ± 0.8	87.8 ± 0.2	48.4 ± 1.2	86.0 ± 0.2	65.5 ± 0.8	94.0 ± 0.1	82.2 ± 0.1
Ensemble	98.6 ± 0.2	59.4 ± 1.4	88.9 ± 0.2	24.3 ± 1.5	88.9 ± 0.2	60.6 ± 3.2	95.2 ± 0.2	84.7 ± 1.4
DUE	98.1 ± 0.1	59.0 ± 2.0	88.6 ± 0.2	24.5 ± 3.1	84.6 ± 1.9	59.6 ± 3.2	88.5 ± 7.8	81.6 ± 4.5
DUQ	96.9 ± 0.1	61.4 ± 1.2	87.4 ± 0.4	41.8 ± 1.5	77.2 ± 0.9	37.2 ± 13.2	91.5 ± 0.3	79.2 ± 3.4
DDU	98.1 ± 0.1	38.3 ± 9.0	89.3 ± 0.1	33.5 ± 9.7	85.5 ± 0.2	34.3 ± 10.9	94.8 ± 0.2	67.7 ± 7.3
SNGP	97.7 ± 0.4	58.9 ± 4.6	86.4 ± 1.4	34.7 ± 3.7	85.5 ± 0.3	64.6 ± 3.0	94.0 ± 0.2	84.5 ± 0.6
MIR	97.6 ± 0.2	72.4 ± 1.1	87.4 ± 0.3	47.4 ± 3.7	85.3 ± 0.2	55.0 ± 5.7	94.1 ± 0.2	71.9 ± 3.1

Table 2: We evaluate the in-domain test accuracy (Acc, %) and calibration performance (rAULC, %) on MNIST, FashionMNIST, CIFAR10 and SVHN datasets. The backbones for all methods are MLP for MNIST/FashionMNIST and ResNet-18 for CIFAR10/SVHN. We observe that - in particular - DUE, SNGP and MIR are well calibrated across several scenarios.

do not only fare well at detecting OOD data but also deliver well calibrated uncertainties under synthetic distributional shifts. However, this is not sufficient to justify their use for real-world safety-critical applications. Refer to Sec. 4.2.3 for an analysis of calibration under realistic distributional shift.

OOD Detection. Tab. 3 shows quantitative results on detecting OOD data for DUMs, MC dropout, softmax entropy and deep ensembles trained on MNIST/FashionMNIST (similarly in the supplement for ResNet-18 trained on CIFAR10/SVHN). Among DUMs, SNGP and MIR demonstrate the best performance across a variety of scenarios. While DUMs confirm to be naturally suited for OOD detection, other established approaches (*e.g.* MC dropout) remain competitive. We note a particular drop in performance for DUMs estimating uncertainty based on the distribution of hidden representations (*i.e.* MIR and DDU) in the case of CIFAR10 vs. SVHN (see supplement). We hypothesize that this results from difficulties of generative models at distinguishing CIFAR10 and SVHN [45].

Method	MNIST \rightarrow F-MNIST		MNIST \rightarrow Omniglot		F-MNIST \rightarrow MNIST		F-MNIST \rightarrow Omniglot	
	AUROC	AUPR	AUROC	AUPR	AUROC	AUPR	AUROC	AUPR
Softmax	89.0 \pm 1.2	88.5 \pm 1.4	95.1 \pm 0.3	94.5 \pm 0.4	73.2 \pm 3.5	75.9 \pm 2.6	75.9 \pm 1.5	74.1 \pm 1.6
Dropout	94.4 \pm 0.9	92.0 \pm 1.8	94.8 \pm 0.2	92.0 \pm 0.5	95.8 \pm 0.2	93.6 \pm 0.6	96.3 \pm 0.2	94.3 \pm 0.3
Ensemble	95.2 \pm 1.0	91.4 \pm 3.6	97.3 \pm 0.4	95.3 \pm 0.1	87.0 \pm 1.5	81.4 \pm 0.3	90.7 \pm 1.1	87.6 \pm 2.5
DUE	90.8 \pm 2.3	90.9 \pm 2.0	94.2 \pm 0.2	92.8 \pm 0.2	68.2 \pm 1.9	65.7 \pm 3.0	72.4 \pm 1.7	65.8 \pm 2.8
DUQ	90.2 \pm 3.0	92.2 \pm 2.4	93.8 \pm 0.3	93.8 \pm 0.4	95.1 \pm 1.1	95.9 \pm 1.0	94.7 \pm 0.6	94.3 \pm 0.7
DDU	83.9 \pm 7.6	83.4 \pm 7.9	75.2 \pm 6.7	69.4 \pm 9.5	90.8 \pm 5.5	92.2 \pm 4.8	90.6 \pm 4.6	90.3 \pm 4.6
SNGP	93.2 \pm 1.2	94.6 \pm 1.3	94.8 \pm 0.7	93.9 \pm 0.7	89.2 \pm 1.1	87.9 \pm 1.3	89.8 \pm 1.7	85.5 \pm 2.7
MIR	97.0 \pm 0.7	97.7 \pm 0.5	97.3 \pm 0.6	97.4 \pm 0.5	99.0 \pm 0.3	99.2 \pm 0.2	97.9 \pm 0.2	97.6 \pm 0.4

Table 3: Experiments for OOD detection (AUROC and AUPR, %). The baseline method and all DUMs use a MLP trained on MNIST/FashionMNIST and predict on another dataset. MIR demonstrates strong performance. (F-MNIST = FashionMNIST).

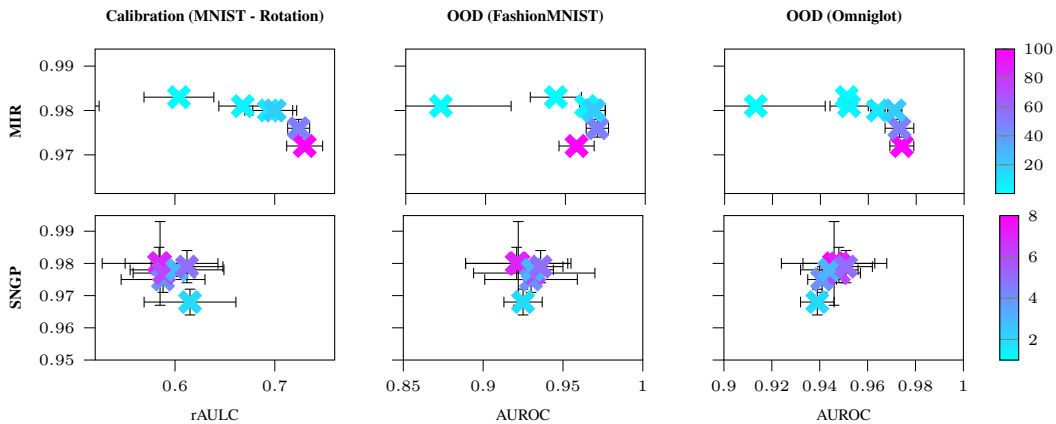


Figure 2: Trained on MNIST. Vertical axis: Test accuracy. Horizontal axis: rAULC (left), AUROC against FashionMNIST (center) and Omniglot (right) for MIR (top) and SNGP (bottom) using different regularization strength. For SNGP a larger hyperparameter corresponds to less regularization. For MIR we observe a correlation between regularization strength and performance.

Sensitivity to Regularization Strength. The hyperparameter associated with each DUM constitutes an important element in each method. It is important to know whether their performance in terms of OOD detection and calibration is sensitive to its choice. Intuitively, we expect the regularization technique to be positively correlated with OOD detection performance, since this is what most DUMs were designed for. For each regularization paradigm - distance-awareness (SNGP) and informative representations (MIR) -, Fig. 2 visualizes the calibration (rAULC) and OOD detection (AUROC) performance depending on the strength of the regularization (similarly for other datasets and methods in the supplement). Most interestingly, we find that DUMs regularizing the Lipschitz constant of the underlying feature extractor do not show evidence for a correlation between the regularization strength and the performance on OOD detection. One possible reason for this result is that Lipschitz-regularization is defined in the context of a particular predefined norm (*e.g.* L_2) (see Sec. 3). However, this norm does not necessarily represent meaningful distances on a particular dataset (*e.g.* images). On the contrary, in the case of enforcing informative representations using reconstruction regularization (MIR), we find evidence for a correlation between regularization strength and performance in terms of both OOD detection and calibration.

4.2 Semantic Segmentation

DUMs have been particularly motivated by prior work from a practical perspective due to their fast inference speed. However, no practical extension of such methods to dense prediction tasks has been proposed yet. This section evaluates whether DUMs seamlessly scale to realistic vision tasks and compares their behaviour under realistic, continuous distributional shifts with MC dropout. Therefore, we choose MIR [28] and SNGP [24], which both demonstrate good performance on uncer-

tainty estimation for image classification and utilize conceptually different underlying regularization techniques, and adapt them to semantic segmentation.

We consider semantic segmentation as a multidimensional classification problem, where for each pixel of the output mask represents an independent classification problem. Given an image \mathbf{x} with n pixels $\mathbf{y} = \{y_1, \dots, y_n\}$, the predictive distribution factorizes according to $p(\mathbf{y} | \mathbf{x}) = p(y_1 | \mathbf{x})p(y_2 | \mathbf{x}) \dots p(y_n | \mathbf{x})$. We are interested in a global uncertainty estimate for the output map as our distributional shifts act on a global scale (see Sec. 4.2.1) and, thus, use the average pixel-level uncertainty as an image-level uncertainty.

While for image classification we simulated domain shift through synthetic distributional shifts, *i.e.* additive Gaussian noise and rotation, for semantic segmentation we are interested in challenging current methods with realistic continuous distributional shifts along natural directions. Sec. 4.2.1 describes the dataset we collected for this purpose. In Sec. 4.2.2 we report architectural choices and we detail how we extended the chosen DUMs to dense prediction tasks. Results and findings are discussed in Sec. 4.2.3.

4.2.1 Dataset

To benchmark our model in a realistically and continuously changing environment, we collect a synthetic dataset for semantic segmentation. We use the CARLA Simulator [61] for rendering the images and segmentation masks. The classes definition is aligned with the CityScape dataset [62].

Training data. Data is collected from four towns in CARLA. We produce 32 sequences from each town. Vehicles and pedestrians are randomly generated for each sequence. Every sequence has 500 frames with a sampling rate of 10 FPS. We uniformly sample a validation set.

Continuous Distributional Shifts. We use the time-of-the-day (weather conditions in the supplement) as the parameter for continuously changing the distribution. Visual examples and details on data collection are in the appendix. The time-of-the-day is parametrized by the Sun’s altitude angle, where 90° means the mid-day (training data) and the 0° means the dusk/dawn. We produce samples with altitude angles from 90° to 15° by steps of 5° , and 15° to -5° , where the environment changes sharply, in 1° steps.

4.2.2 Method Details

Backbone. We adopt Dilated ResNet (DRN) [63, 64] as semantic segmentation backbone. DRN introduces dilated convolutions to ResNet, effectively increasing the receptive field without increasing the number of layers or parameters. This improves the spatial accuracy of DRN, achieving satisfactory results on CityScapes [62]. We adopt the variant DRN-A-50. All experiments were run 3 times.

SNGP. DRN uses 1×1 convolutions at the last layer to map the latest feature map to the predicted segmentation mask. This works under the assumption that all pixels in the output mask are i.i.d. random variables. Following this intuition, we extend SNGP to semantic segmentation by fitting a $GP : \mathbb{R}^Z \rightarrow \mathbb{R}^C$ at pixel level that maps from the deep feature dimension z to the number of classes c . By keeping the GP kernel parameters shared across all pixels, we simulate a 1×1 convolutional GPs, *i.e.* $\sigma : (H_l \times W_l \times Z) \rightarrow (H_l \times W_l \times C)$, where σ convolves the GP, H_l and W_l are respectively feature map height and width at layer l , Z is the number of latent features and C is the number of output classes. For details about the GP we refer to [24] or the supplement.

MIR. To estimate image-level uncertainty MIR requires fitting the distribution of hidden representations. We fit a Gaussian mixture model (GMM) with 20 components (*i.e.* number of classes) to each spatial location of the hidden representations using features extracted from the training data independently. This assumes that the distribution is translation invariant and factorizes along the spatial dimensions of the latent space which is similar to the procedure used in [65]. We refer to the supplement for more details and computation of pixel-level uncertainties in this framework.

4.2.3 Results

Continuous Distribution Shift. We compare DUMs with MC dropout and the softmax baseline. in terms of their calibration under realistic distributional shifts. Tab. 4 shows quantitative results. Encouragingly, all methods yield similar performance in terms of mean Intersection over Union (mIoU) and pixel accuracy. However, we observe that while DUMs yield a considerable improvement

Method		Softmax	MCD	SNGP	MIR
In-domain Testset	Acc (%)	93.0 ± 0.1	92.9 ± 0.1	93.2 ± 0.1	93.0 ± 0.1
	mIoU (%)	44.3 ± 0.4	44.0 ± 0.4	44.4 ± 0.0	44.2 ± 0.0
Time-of-the-Day	rAULC	25.9 ± 3.1	91.2 ± 1.2	66.7 ± 4.1	72.5 ± 4.1

Table 4: We compare predictive performance on unperturbed test data - pixel accuracy (Acc.) and mIoU - and calibration (rAULC) on realistic continuous distributional shifts of softmax, MC dropout (MCD), SNGP and MIR on semantic segmentation. While SNGP and MIR perform better than the simple softmax baseline, they remain outclassed by MC dropout in terms of calibration.

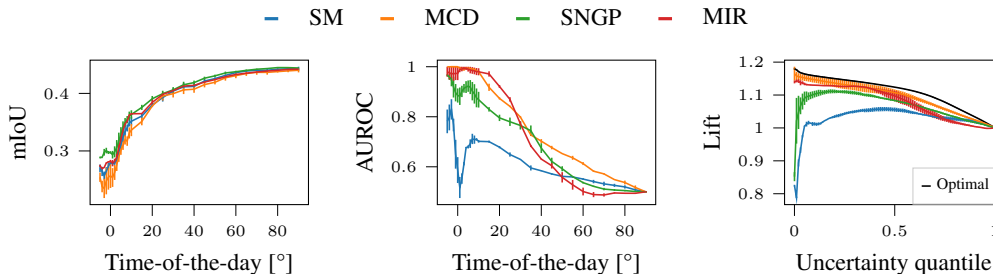


Figure 3: We compare the mIoU (left), AUROC (center) and rAULC (right) of softmax (SM), MC dropout (MCD), SNGP and MIR under realistic continuous distributional shifts. The AUROC is computed against unperturbed test data. While the softmax entropy as a measure of uncertainty clearly fails in this scenario, DUMs (SNGP/MIR) yield reasonable uncertainty using a similar computational budget at identical predictive performance (mIoU). However, MC dropout, with its larger computational footprint, provides better calibrated uncertainty estimates (Lift).

over the softmax entropy - both in OOD detection and calibration - using a similar computational budget, these methods still fall short of established approaches, such as MC dropout, in terms of calibration under challenging realistic distributional shifts. This finding is further supported by the results of Fig. 3, which shows that DUMs behave poorly in terms of calibration (see Lift curves) under realistic distributional shift. We believe that these shortcomings must be addressed before practical deployment.

5 Conclusion

While DUMs show good OOD detection performance and are interesting for practical applications in need of efficient uncertainty quantification, we find them struggling regarding calibration under realistic distributional shifts. Despite promising results of uncertainty on toy datasets, this does not extrapolate to more realistic scenarios (Sec. 4.2). We find that, while DUMs outperform the softmax entropy, MC dropout clearly outperforms DUMs regarding uncertainty calibration.

Moreover, another desirable property for such methods would be that the strength of the feature space regularization correlates with the quality of OOD detection. However, this is not verified for Lipschitz regularization by our investigation. We hypothesize that this originates from the choice of metric for regularization - *i.e.* L_2 distance - which is not meaningful in the image space. We hope that our findings will foster future research on making these promising family of methods better calibrated and more broadly applicable.

6 Broader Impact

Efficient uncertainty estimation is a prerequisite for the deployment of machine learning in safety-critical applications with real-time decision-making, such as autonomous driving or robotics applications. Advancements in uncertainty estimation can encourage adoption of machine learning solutions across a broad spectrum of applications, with consequences on the safety of both workers and final users of autonomous systems. We hope that our work will foster future research to mitigate effects of skewed training data, *e.g.* underrepresented minorities, further increasing the adoption of machine learning in decision-making agents.

7 Appendix

We provide implementation and optimization details, additional results, comparisons and ablation studies. In particular, Sec. 7.2.1/Sec. 7.2.2 show additional results for image classification/semantic segmentation. Moreover, Sec. 7.3 gives an explanation of the Lipschitz regularization techniques used in this work. We report optimization/implementation details in Sec. 7.4/Sec. 7.5. Furthermore, we describe the quantification of uncertainty for image classification Sec. 7.5.3 and semantic segmentation Sec. 7.5.4. Finally, we provide details on the data collection process in CARLA and examples from the sequences collected for semantic segmentation Sec. 7.6.

7.1 Official Implementation

An official implementation of this work can be found, completely anonymized, at the following link: https://1drv.ms/u/s!AmvoAvndzeKvarxW2fCTi_4W9-o?e=KjaQNE

7.2 Additional Results

7.2.1 Image Classification

OOD Detection. Tab. 5 show quantitative results on detecting OOD data for DUMs, MC dropout, softmax entropy and deep ensembles trained on CIFAR/SVHN. Similarly to the results shown in Sec. 4.1.1, among DUMs SNGP and MIR demonstrate strong performance across a variety of scenarios. Note that in this case DUE also shows good performance. While DUMs confirm to be naturally suited for OOD detection, other established approaches (*e.g.* MC dropout) remain competitive.

Method	CIFAR10 → SVHN		CIFAR10 → STL10		SVHN → CIFAR10		SVHN → STL10	
	AUROC	AUPR	AUROC	AUPR	AUROC	AUPR	AUROC	AUPR
Softmax	83.1 ± 1.0	77.2 ± 1.8	67.4 ± 1.3	71.5 ± 1.2	93.1 ± 0.5	97.5 ± 0.2	93.6 ± 0.6	98.1 ± 0.2
Dropout	85.2 ± 0.9	76.5 ± 1.2	68.7 ± 0.3	72.8 ± 0.5	94.3 ± 0.4	98.0 ± 0.1	94.7 ± 0.3	98.5 ± 0.1
Ensemble	79.8 ± 2.9	97.6 ± 1.7	98.2 ± 1.8	85.8 ± 3.4	99.3 ± 1.1	97.7 ± 3.5	98.3 ± 0.5	96.8 ± 2.3
DUE	84.3 ± 4.7	77.4 ± 7.3	71.3 ± 2.6	75.5 ± 3.0	92.2 ± 3.3	97.0 ± 1.4	92.4 ± 3.5	97.7 ± 1.2
DUQ	76.8 ± 5.0	67.2 ± 6.3	65.1 ± 1.9	70.8 ± 1.0	90.1 ± 1.2	96.3 ± 0.4	91.1 ± 1.5	97.3 ± 0.4
DDU	69.0 ± 6.3	51.1 ± 7.4	68.9 ± 3.6	72.8 ± 3.2	73.4 ± 5.5	89.8 ± 2.4	76.7 ± 5.4	92.5 ± 2.0
SNGP	85.3 ± 4.7	79.4 ± 6.5	76.1 ± 1.7	79.4 ± 1.5	95.8 ± 0.3	98.4 ± 0.1	96.4 ± 0.3	98.9 ± 0.1
MIR	85.0 ± 6.0	71.4 ± 11.7	72.2 ± 2.1	<u>76.3 ± 2.0</u>	91.6 ± 1.2	97.0 ± 0.4	92.8 ± 1.2	97.9 ± 0.3

Table 5: Experiments for OOD detection performance (AUROC and AUPR, %). The baselines and all DUMs use a ResNet-18 trained on CIFAR10/SVHN. In particular, SNGP, MIR and DUE demonstrate strong performance. However, computationally more expensive baselines remain competitive.

Sensitivity to regularization strength. We provide additional ablation studies on the sensitivity to regularization strength for different methods on datasets, *i.e.* MNIST (Fig. 4), FashionMNIST (Fig. 5), CIFAR10 (Fig. 6), and SVHN (Tab. 6). These results confirm the findings of the main manuscript, *i.e.* that only MIR and Dropout are sensible to regularization strength, while DUMs based on Lipschitz regularization are not influenced by the regularization strength. Note that for MIR we observe that regularization strength and calibration/ood detection are anti-correlated. We hypothesize that this originates from generative models inability to distinguish these datasets [45]. Thus, storing more information in the latent representations about the input leads to worse OOD detection performance.

7.2.2 Semantic Segmentation

Weather conditions. Additionally, we evaluate the calibration performance of DUMs under changing weather conditions. Fig. 10 of Sec. 7.6 demonstrates examples of this distributional shift. The quantitative evaluation results are summarized in Table 7. Similar to the trend in the Table 4, all methods yield decent performance on pixel accuracy and mIoU, and the DUMs obtain significant improvements over the Softmax baseline. However, we again observe that MC dropout outperforms DUMs on continuous distributional shifts.

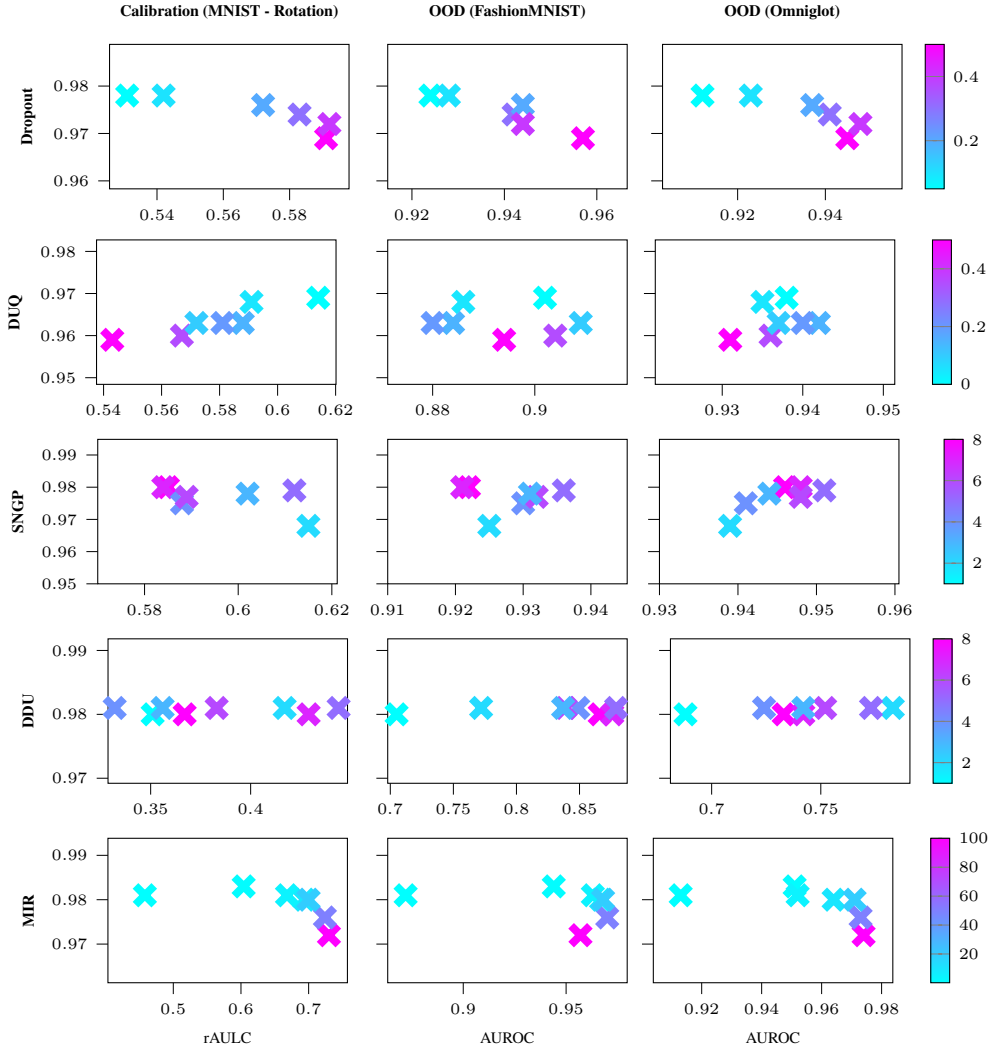


Figure 4: Trained on MNIST. Vertical axis: Test accuracy. Horizontal axis: rAULC (left), AUROC against FashionMNIST (center) and Omniglot (right) for Dropout (1st row), DUQ (2nd row), SNGP (3rd row), DDU (4th row) and MIR (5th row) using different regularization strength. For SNGP a larger hyperparameter corresponds to less regularization. For Dropout and MIR we observe a correlation between regularization strength and performance.

Examples of segmentation and uncertainty masks. We show qualitative examples of predicted masks, error masks and uncertainty masks for Softmax, MC dropout, SNGP and MIR on semantic segmentation. Fig. 7 illustrates examples under *minimal* distributional shift (*i.e.* Azimuth angle of the sun = 85°) and Fig. 8 under *maximal* distributional shift (*i.e.* Azimuth angle of the sun = -5°). We show the input image (Input), the segmentation ground truth (GT), the predicted segmentation mask (Prediction), the error mask (Error) and the uncertainty mask (Uncertainty). The error mask is computed as a boolean mask with True values when a pixel is predicted wrongly (yellow) and False (blue) when the prediction is instead correct. The uncertainty mask is preprocessed to facilitate visualization. In particular, we first compute mean μ and standard deviation σ of per-pixel uncertainties over each uncertainty mask. Then, the uncertainty mask is clipped between $[\mu - 2\sigma, \mu + 2\sigma]$. Finally, the uncertainty mask is normalized between 0 and 1 before being visualized.

While the softmax entropy provides decent uncertainty estimates under minimal distributional shift, it tends to be overconfident under severe distributional shift. In particular, Softmax models are only uncertain close to object borders, but they are confident about large portions of the image that are instead predicted wrongly. This can be observed in Fig. 8, where all models tend to predict the entire

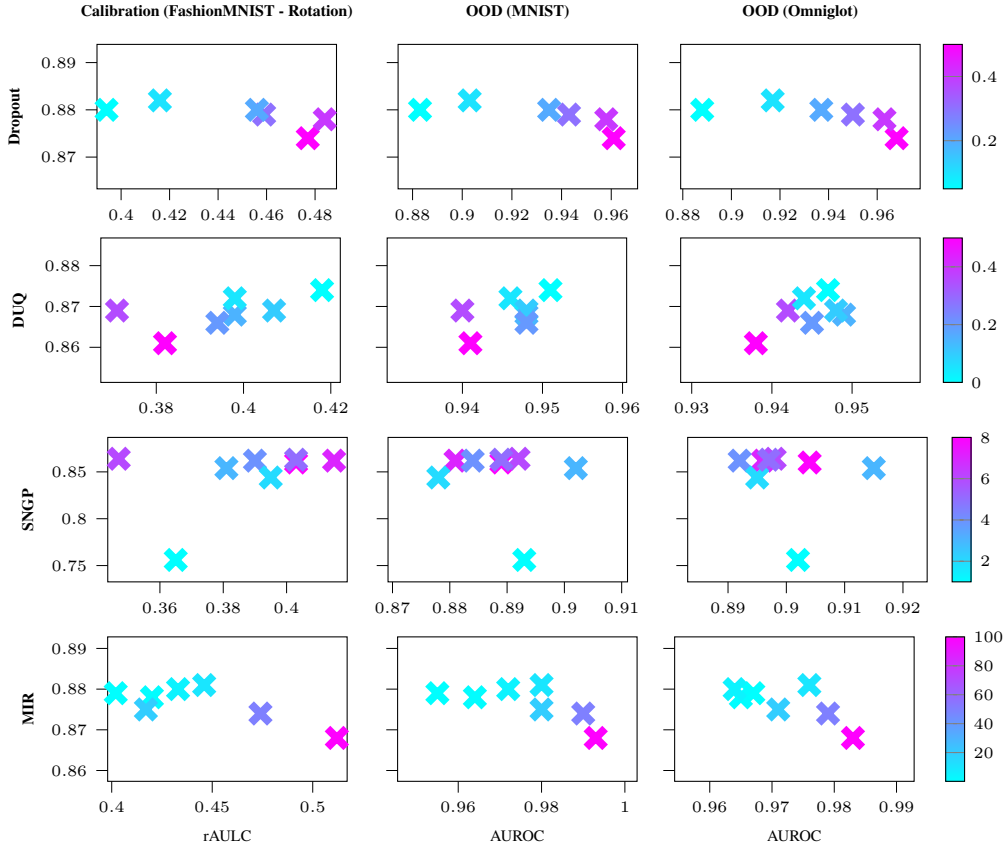


Figure 5: Trained on FashionMNIST. Vertical axis: Test accuracy. Horizontal axis: rAULC (left), AUROC against MNIST (center) and Omniglot (right) for Dropout (1st row), DUQ (2nd row), SNGP (3rd row) and MIR (4th row) using different regularization strength. For SNGP a larger hyperparameter corresponds to less regularization. For Dropout and MIR we observe a correlation between regularization strength and performance.

sky wrongly (assigned to ‘building’ class), but the Softmax model is the most confident about its predictions of the sky being correct. DUMs and MC dropout do a better job at recognizing wrong predictions under sever domain shift by outputting higher uncertainty values.

7.3 Lipschitz Regularization

Gradient Penalty. Given a model g and an input x , regularising the Frobenius norm $\|J\|_F$ of its Jacobian J constrains its Lipschitz constant. Therefore, the following two-sided gradient penalty is used: $\lambda [\|\nabla_x g(x)\|_F - 1]^2$, where λ is the regularization strength, $\|\cdot\|_2$ is the L_2 norm, the target bi-Lipschitz constant is 1.

Spectral Normalization. A more efficient technique to constrain the Lipschitz constant is SN [36]. For each layer $g : \mathbf{h}_{in} \rightarrow \mathbf{h}_{out}$, SN effectively constrain its Lipschitz norm $\|g\|_{Lip} = \sup_{\mathbf{h}} sn(\nabla g(\mathbf{h}))$, where $sn(A)$ is the spectral norm - the L_2 matrix norm - of the matrix A , equivalent to its largest singular value. When applied, SN normalizes the spectral norm of the weights W of each layer to satisfy the soft-Lipschitz constraint $sn(W) = c$ (hard- if the Lipschitz constant $c = 1$): $W_{sn} = W/sn(W)$. A number of DUMs - SNGP [24], DUE [25] and DDU [26] - rely on SN of the weight matrices to make the feature extractor distance preserving.

7.4 Training Details

We provide training and optimization details for all evaluated methods. All methods using spectral normalization use 1 power iteration. Hyperparameters were chosen to minimize the validation loss.

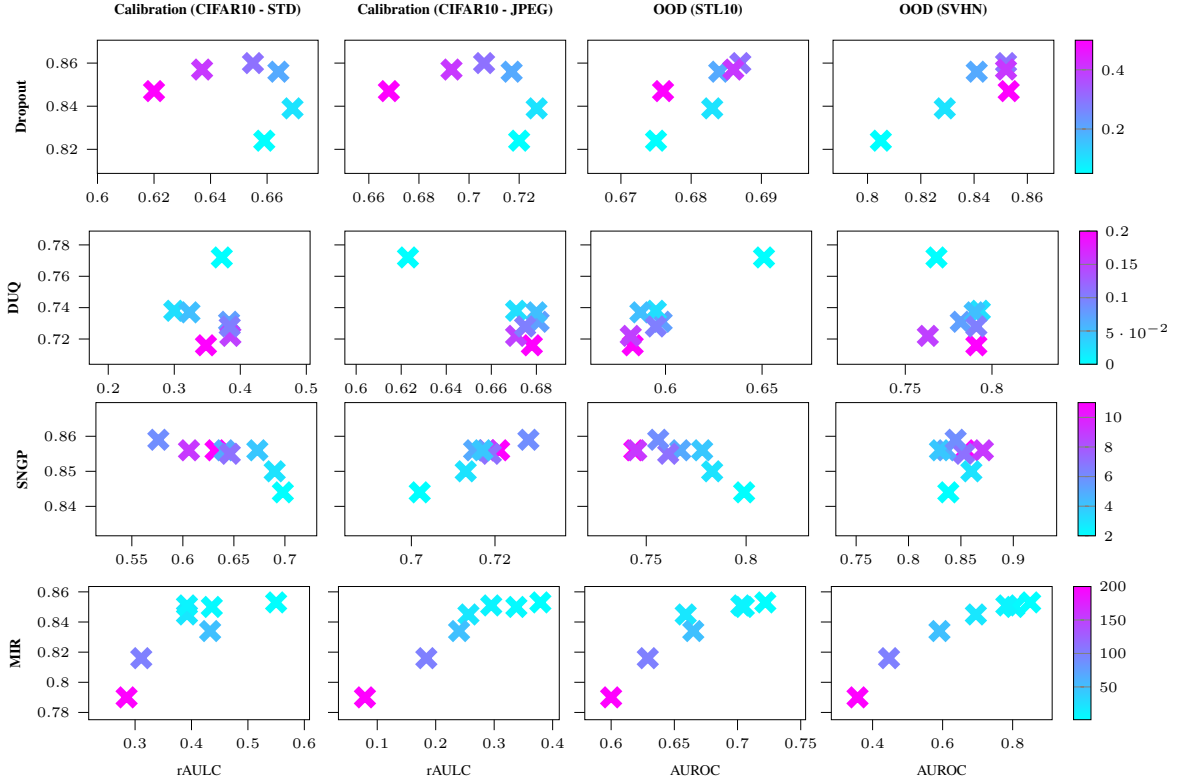


Figure 6: Trained on CIFAR10. Vertical axis: Test accuracy. Horizontal axis: rAULC against additive gaussian noise (1st column) and additive jpeg quality corruption (2nd column), AUROC against STL10 (3rd column) and SVHN (4th column) for Dropout (1st row), DUQ (2nd row), SNGP (3rd row) and MIR (4th row) using different regularization strength. For SNGP a larger hyperparameter corresponds to less regularization. For Dropout we observe a correlation between regularization strength and performance.

7.4.1 Image Classification - MNIST/FashionMNIST

All methods trained on MNIST/FashionMNIST used a MLP as backbone with 3 hidden layers of 100 dimensions each and ReLU activation functions. We used a batch size of 128 samples and trained for 200 epochs. No data augmentation is performed.

Softmax and Deep ensembles. We used for the single softmax model the Adam optimizer with learning rate 0.003, and L_2 weight regularization 0.0001. When using ensembles, 10 models are trained from different random initializations.

MC dropout. We used for all baselines the Adam optimizer with learning rate 0.003, dropout rate 0.4 and L_2 weight regularization 0.0001.

DUE We trained DUE with the SGD optimizer with learning rate 0.01, L_2 weight regularization 0.0005, and a multi-step learning rate decay policy with decay rate 0.2 and decay steps at the epochs 60, 120, 160. We found the optimal SN coefficient to be 7, with the GP approximation using 10 (number of classes) inducing points initialized using k-means over 10000 samples.

DUQ We trained DUQ with the SGD optimizer with learning rate 0.01, L_2 weight regularization 0.0001, and a multi-step learning rate decay policy with decay rate 0.3 and decay steps at the epochs 10, 20. Lengthscale for the RBF kernel is 0.1 and optimal gradient penalty loss weight is 0.

DDU. We trained DDU with the Adam optimizer with learning rate 0.001, L_2 weight regularization 0.0001, and a multi-step learning rate decay policy with decay rate 0.2 and decay steps at the epochs 100, 200, 300. We found the optimal SN coefficient to be 6. The GMM fit on top of the pretrained feature extractor is trained for 100 epochs and is fit with 64 batches.

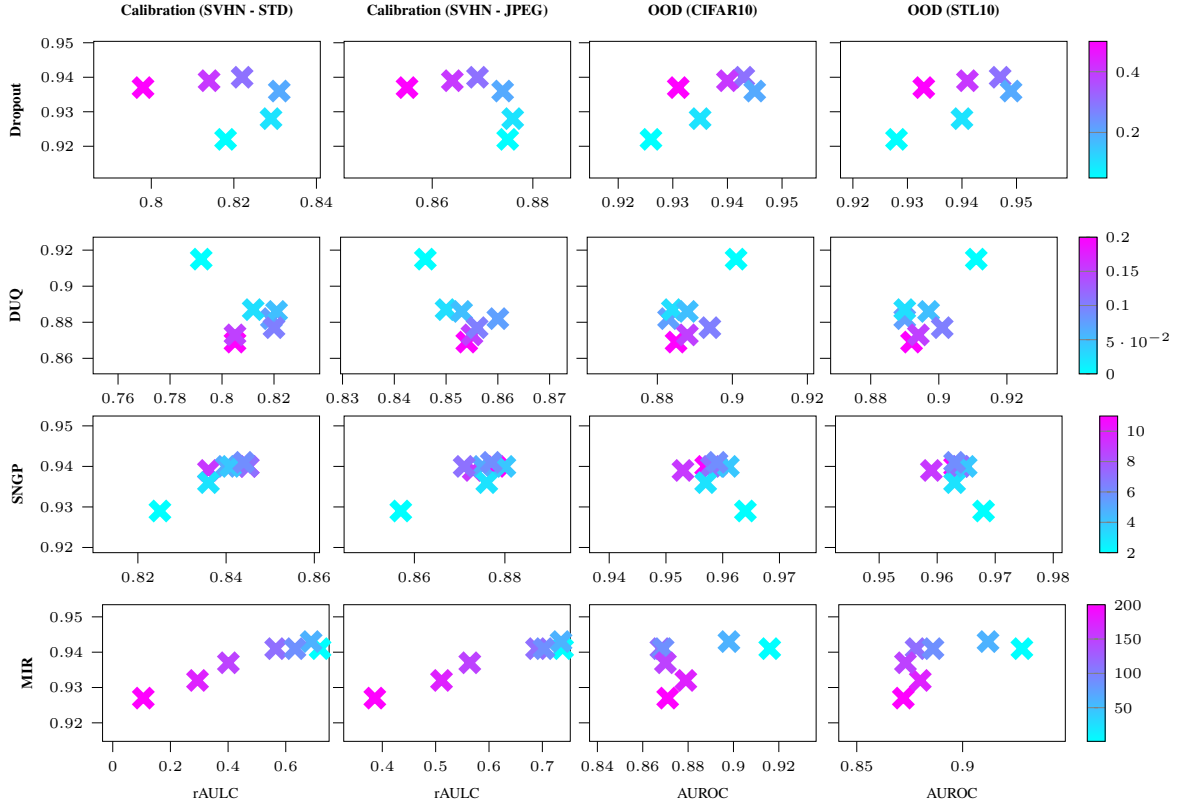


Table 6: Trained on SVHN. Vertical axis: Test accuracy. Horizontal axis: rAULC against additive gaussian noise (1st column) and additive jpeg quality corruption (2nd column), AUROC against CIFAR10 (3rd column) and STL10 (4th column) for Dropout (1st row), DUQ (2nd row), SNGP (3rd row) and MIR (4th row) using different regularization strength. For SNGP a larger hyperparameter corresponds to less regularization. For Dropout we observe a correlation between regularization strength and performance.

Method		Softmax	Dropout	SNGP	MIR
In-domain Testset	Acc (%)	93.0 ± 0.1	92.9 ± 0.1	93.2 ± 0.1	93.0 ± 0.1
	mIoU (%)	44.3 ± 0.4	44.0 ± 0.4	44.4 ± 0.0	44.2 ± 0.0
Weather Conditions	RAULC ($\cdot 10^3$)	70.8 ± 2.6	86.1 ± 0.5	81.3 ± 1.2	72.6 ± 0.5

Table 7: Calibration results on semantic segmentation for weather conditions.

SNGP. We trained SNGP with the SGD optimizer with learning rate 0.05, L_2 weight regularization 0.0003, and a multi-step learning rate decay policy with decay rate 0.2 and decay steps at the epochs 60, 120, 160. We found the optimal SN coefficient to be 6, with the GP approximation using 10 hidden dimensions, lengthscale 2 and mean field factor 30.

MIR. We trained MIR with the Adam optimizer with learning rate 0.001, and L_2 weight regularization 0.0001. We found the optimal reconstruction loss weight to be 1.

7.4.2 Image Classification - CIFAR10/SVHN

When training on CIFAR-10/SVHN, we use a ResNet-18 [60] as backbone. The dimensionality of the last feature space encoded with the ResNet backbone is 100 for all methods. We used a batch size of 128 samples and trained for 400 epochs. The training set is augmented with common data augmentation techniques. We apply random horizontal flips, random brightness augmentation with maximum delta 0.2 and random contrast adjustment with multiplier lower bound 0.8 and upper bound 1.2.

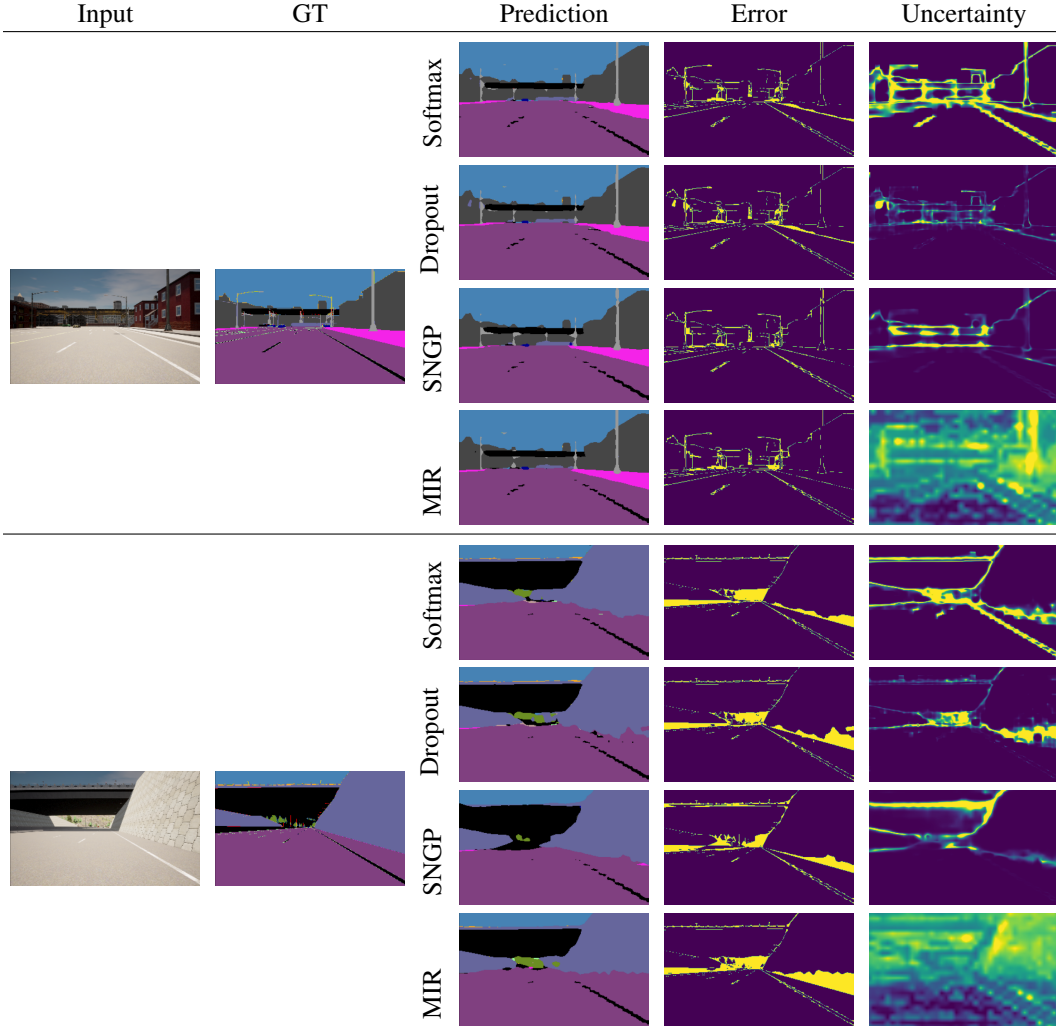


Figure 7: Qualitative comparison of uncertainty from Softmax, MC Dropout, SNGP and MIR under minimal time-of-the-day distribution shift (*i.e.* Azimuth angle of the sun = 85°). We show the input image (Input) and the ground truth mask (GT), and we report for each method the predicted segmentation mask (Prediction), the error mask (Error) and the uncertainty mask (Uncertainty).

Softmax and Deep ensembles. We used for the single softmax model the Adam optimizer with learning rate 0.003, L_2 weight regularization 0.0001, and a multi-step learning rate decay policy with decay rate 0.2 and decay steps at the epochs 250, 300, 400. When using ensembles, 10 models are trained from different random initializations.

MC dropout. We used for all baselines the Adam optimizer with learning rate 0.003, dropout rate 0.3, L_2 weight regularization 0.0001, and a multi-step learning rate decay policy with decay rate 0.2 and decay steps at the epochs 250, 300, 400.

DUE We trained DUE with the SGD optimizer with learning rate 0.01, L_2 weight regularization 0.0005, dropout rate 0.1, and a multi-step learning rate decay policy with decay rate 0.2 and decay steps at the epochs 100, 200, 300. We found the optimal SN coefficient to be 7 for SVHN and 9 for CIFAR-10, with the GP approximation using 10 (number of classes) inducing points initialized using k-means over 10000 samples.

DUQ We trained DUE with the SGD optimizer with learning rate 0.01, L_2 weight regularization 0.0001, dropout rate 0.1, and a multi-step learning rate decay policy with decay rate 0.3 and decay steps at the epochs 200, 250, 300. Lengthscale for the RBF kernel is 0.1 and optimal gradient penalty loss weight is 0

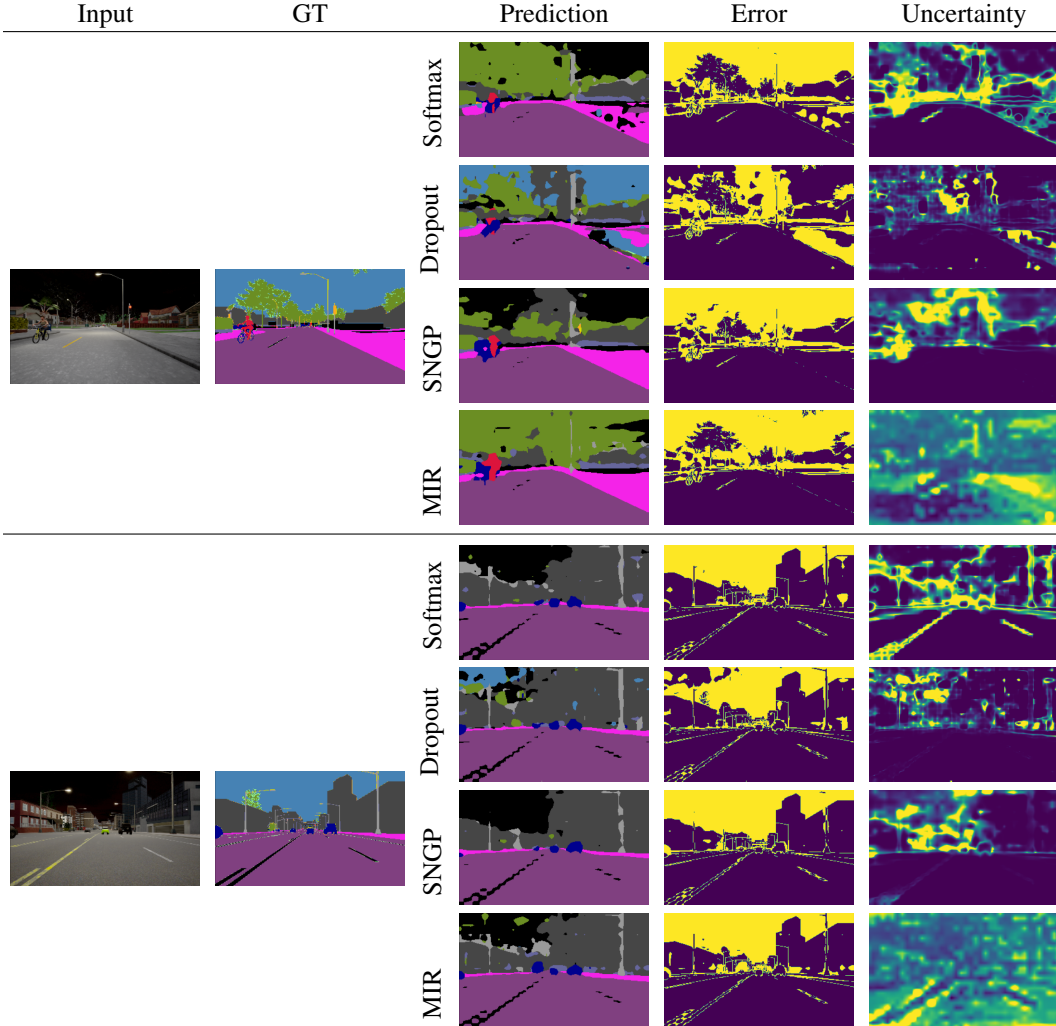


Figure 8: Qualitative comparison of uncertainty from Softmax, MC Dropout, SNGP and MIR under maximal time-of-the-day distribution shift (*i.e.* Azimuth angle of the sun = -5°). We show the input image (Input) and the ground truth mask (GT), and we report for each method the predicted segmentation mask (Prediction), the error mask (Error) and the uncertainty mask (Uncertainty).

DDU. We trained DDU with the Adam optimizer with learning rate 0.001, L_2 weight regularization 0.0001, dropout rate 0.3, and a multi-step learning rate decay policy with decay rate 0.2 and decay steps at the epochs 80, 120, 180. We found the optimal SN coefficient to be 7. The GMM fit on top of the pretrained feature extractor is trained for 100 epochs and is fit with 64 batches.

SNGP. We trained SNGP with the SGD optimizer with learning rate 0.05, L_2 weight regularization 0.0004, dropout rate 0.1, and a multi-step learning rate decay policy with decay rate 0.2 and decay steps at the epochs 100, 200, 300. We found the optimal SN coefficient to be 7, with the GP approximation using 10 hidden dimensions, lengthscale 2 and mean field factor 30.

MIR. We trained MIR with the Adam optimizer with learning rate 0.003, L_2 weight regularization 0.0001, dropout rate 0.1, and a multi-step learning rate decay policy with decay rate 0.2 and decay steps at the epochs 150, 200, 250, 300. We found the optimal reconstruction loss weight to be 1.

7.4.3 Semantic Segmentation.

When training on semantic segmentation, we use a DRN [63, 64] (DRN-A-50) as backbone. We used a batch size of 8 samples and trained for 200 epochs. Images are rescaled to size 200×320 . The training set is augmented with common data augmentation techniques. All training samples

are augmented with random cropping with factor 0.8. We apply random horizontal flips, random brightness augmentation with maximum delta 0.2 and random contrast adjustment with multiplier lower bound 0.8 and upper bound 1.2.

Softmax. We used for the single softmax model the Adam optimizer with learning rate 0.0004, L_2 weight regularization 0.0001, and a multi-step learning rate decay policy with decay rate 0.3 and decay steps at the epochs 30, 60, 90, 120.

MC dropout. We used for all baselines the Adam optimizer with learning rate 0.0004, dropout rate 0.4, L_2 weight regularization 0.0001, and a multi-step learning rate decay policy with decay rate 0.3 and decay steps at the epochs 30, 60, 90, 120.

SNGP. We trained SNGP with the SGD optimizer with learning rate 0.0002, L_2 weight regularization 0.0003, dropout rate 0.1, and a multi-step learning rate decay policy with decay rate 0.2 and decay steps at the epochs 20, 40, 60, 80, 100. We found the optimal SN coefficient to be 6, with the GP approximation using 128 hidden dimensions, lengthscale 2 and mean field factor 25.

MIR. We trained MIR with the Adam optimizer with learning rate 0.0002, L_2 weight regularization 0.0001, dropout rate 0.1, and a multi-step learning rate decay policy with decay rate 0.3 and decay steps at the epochs 30, 60, 90, 120. We found the optimal reconstruction loss weight to be 1.

7.5 Implementation Details.

All methods were re-implemented in Tensorflow 2.0. We payed attention to all the details reported in each paper and we run all experiments for each method multiple times to account for stochasticity, *i.e.* 5 times for classification and 3 times for segmentation. When an implementation was publicly available, we relied on it. This is the case for DUQ (<https://github.com/y0ast/deterministic-uncertainty-quantification>), SNGP (<https://github.com/google/uncertainty-baselines/blob/master/baselines/imagenet/sngp.py>) and DUE (<https://github.com/y0ast/DUE>).

SNGP. We follow the publicly available implementation of SNGP, which, compared to the implementation described in the original paper, proposes to further reduce the computational overhead of the GP approximation by replacing the Monte-Carlo averaging with the mean-field approximation [66]. This is especially relevant in large-scale tasks like semantic segmentation, were it is important to reduce the computational overload.

7.5.1 Image Classification

DUE. Note that only DUE uses a SN approximation also for the batch normalization layer. All other methods only restrict the Lipschitz constant of convolutional and fully connected layers.

MIR only differs from regular softmax models in its decoder module used for the reconstruction regularization loss [28]. When training MLP architectures the decoder is comprised of two fully-connected layer. The first has a ReLU activation function and 200 output neruons. The second has a linear activation function and its output dimensionality equals that of the models' input data. When training convolutional neural networks the decoder is comprised of four blocks of transpose convolutions, batch normalization layers and ReLU activation functions that gradually upscale the hidden representations to the dimensionality of the input data. These four blocks are followed by a 1x1 convolution with linear activation function.

7.5.2 Semantic Segmentation

MIR. Similar to image classification, MIR only differs from regular segmentation models in its decoder module used for the reconstruction regularization loss [28]. The decoder module is comprised of a single point-wise feed forward layer that maps the hidden representations $\mathbf{z} \in \mathbb{R}^{W_z \times H_z \times C_z}$ to $\mathbf{z} \in \mathbb{R}^{W_z \times H_z \times 3}$. Subsequently, the result is bilinearly upsampled to the image resolution on which we compute the reconstruction loss.

7.5.3 Uncertainty Derivation.

We provide details on the estimation of uncertainty for the baseline methods. For details on the uncertainty derivation in DUMs, please refer to Sec. 3 of the main paper or to the original paper of each analysed method.

Softmax. In case of the softmax baseline we estimate uncertainty using the entropy of the predictive distribution parameterized by the neural network. Given an input \mathbf{x} the entropy H is given by $H(\mathbf{y}|\mathbf{x}) = \sum -p(\mathbf{y}|\mathbf{x}) \log(p(\mathbf{y}|\mathbf{x}))$ where $p(\mathbf{y}|\mathbf{x})$ are the softmax probabilities.

MC dropout and deep ensembles. We following [67] and compute epistemic uncertainty as the conditional mutual information between the weights \mathbf{w} and the predictions \hat{y} given the input \mathbf{x} . Given an input \mathbf{x} and a set of weights \mathbf{w} we observe the predictive distribution $p(\hat{y}|x, w)$. Then epistemic uncertainty u_{ep} is calculated by approximating the mutual information conditioned on the input \mathbf{x} :

$$\begin{aligned} u_{ep} &= I(\hat{y}, w|x) \\ &= H(\hat{y}|x) - H(\hat{y}|w, x) \\ &= E_{y \sim p(\hat{y}|x)} [-\log(p(\hat{y}|x))] - u_{al} \end{aligned}$$

where u_{al} denotes the aleatoric uncertainty. Here, $p(\hat{y}|x) = \int dw p(w) p(\hat{y}|x, w)$ is evaluated using a finite set of samples/ensemble members.

7.5.4 Uncertainty Derivation for Semantic Segmentation.

We derive uncertainty estimates for each method for semantic segmentation. We average pixel-level uncertainties under the assumption that all pixels are represented by i.i.d. variables.

Uncertainty Averaging. In our experiments on continuous distributional shifts we want to estimate a global uncertainty for the output map and are not interested in pixel-level confidence. Therefore, we propose to approximate the uncertainty of the predicted segmentation masks as the average of all pixel-level uncertainties, i.e.,

$$\begin{aligned} H(\mathbf{y} | \mathbf{x}) &= \mathbb{E}_{\mathbf{x}} \left[- \int_{\mathbf{y}} p(\mathbf{y} | \mathbf{x}) \log p(\mathbf{y} | \mathbf{x}) d\mathbf{y} \right] \\ &= \mathbb{E}_{\mathbf{x}} \left[- \int_{\mathbf{y}} p(\mathbf{y} | \mathbf{x}) \log p(y_1 | \mathbf{x}) d\mathbf{y} \right] + \dots + \mathbb{E}_{\mathbf{x}} \left[- \int_{\mathbf{y}} p(\mathbf{y} | \mathbf{x}) \log p(y_n | \mathbf{x}) d\mathbf{y} \right] \\ &\approx \frac{1}{n} \sum_{i=1}^n H(y_i | \mathbf{x}) \end{aligned} \tag{1}$$

MIR estimates epistemic uncertainty using the likelihood of hidden representations $\mathbf{z} \in \mathbb{R}^{W_z \times H_z \times C_z}$. Since \mathbf{z} is high-dimensional in our experiments, we assume that it factorizes along W_z and H_z and is translation invariant. Formally, $p(\mathbf{z}) = \prod_i^{W_z} \prod_j^{H_z} p_{\theta}(\mathbf{z}_{ij})$ where $\mathbf{z}_{ij} \in \mathbb{R}^{W_z \times H_z}$ and θ is shared across W_z and H_z .

We parameterize p_{θ} with a GMM with $n = 10$ components where each component has a full covariance matrix. We fit the GMM on 100000 hidden representations ($\mathbf{z}_{ij} \in \mathbb{R}^{C_z}$) randomly picked from the training dataset post-training. Since $C_z = 1024$ is still high-dimensional, we first apply PCA to reduce its dimensionality to 32.

In the dilated resnet architecture used for semantic segmentation the latent representation \mathbf{z} is passed through a point-wise feedforward layer $f : \mathbb{R}^{W_z \times H_z \times C_z} \mapsto \mathbb{R}^{W_z \times H_z \times 3}$ and, subsequently, bilinearly upsampled to image resolution ($\mathbb{R}^{W \times H \times K}$) where K is the number of classes. We could estimate the global, i.e. image-level, uncertainty of an input, by providing the negative log-likelihood of the factorizing distribution. However, in order to also obtain pixel-wise uncertainties using MIR, we first compute the negative log-likelihood (i.e. epistemic uncertainty) associated with each latent representation \mathbf{z}_{ij} . Then, we bilinearly upsample the negative log-likelihoods and use the result as proxy for pixel-wise epistemic uncertainty. To obtain a global, i.e. image-level, uncertainty we apply the same averaging scheme used for SNGP, softmax and MC dropout.

7.6 Dataset

To benchmark our model on data with realistically and continuously changing environment, we collect a synthetic dataset for semantic segmentation. We use the CARLA Simulator [61] for rendering the images and segmentation masks. The classes definition is aligned with the CityScape dataset [62]. In order to obtain a fair comparison, all the OOD data are sampled with the same trajectory and the environmental objects, except for the time-of-the-day or weather parameters.

In-domain data The data is collected from 4 towns in CARLA. We produce 32 sequences from each town. The distribution of the vehicles and pedestrians are randomly generated for each sequence. Every sequence has 500 frames with a sampling rate of 10 FPS. From them we randomly sample the training and validation set.

Out-of-domain data Here, we consider the time-of-the-day and the rain strength as the parameters for the continuous changing environment. In practice, these two parameters have major influence for autonomous driving tasks.

The change of the time-of-the-day is illustrated in Fig. 9. The time-of-the-day is parametrized by the Sun’s altitude angle, where 90° means the mid-day and the 0° means the dusk or dawn. Here, we produce samples with the altitude angle changes from 90° to 15° by step of 5° , and 15° to -5° by step of 1° where the environment changes shapely. From these examples, we can confirm that the change of time-of-the-day leads to the major change in the lightness, color and visibility of the sky, roads and the buildings nearby. The effect of rain strength is demonstrated in Fig. 10. Here the cloudiness and, ground wetness and ground reflection are the main changing parameters.

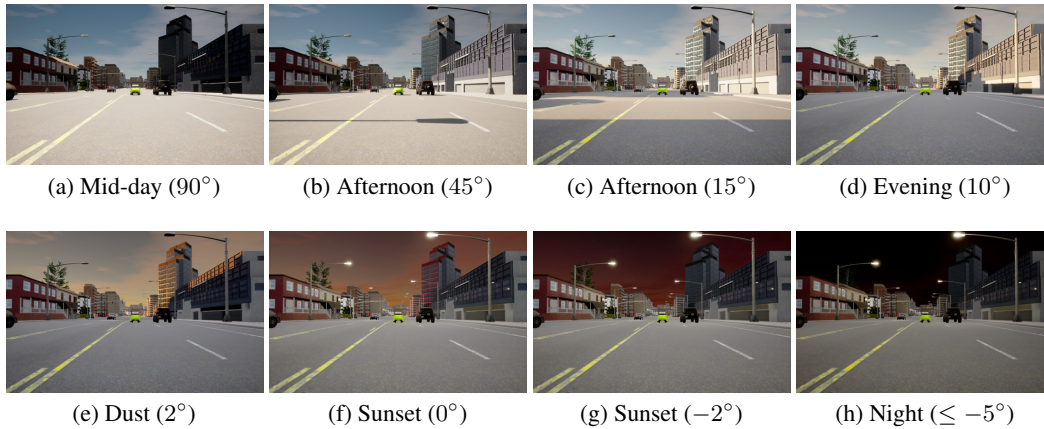


Figure 9: Changing of the time-of-the-day

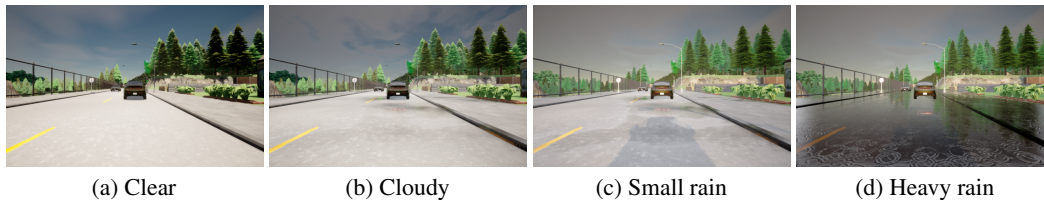


Figure 10: Changing of the weather

References

- [1] Gilles Blanchard, Gyemin Lee, and Clayton Scott. Generalizing from several related classification tasks to a new unlabeled sample. *Advances in neural information processing systems*, 24:2178–2186, 2011.
- [2] Krikamol Muandet, David Balduzzi, and Bernhard Schölkopf. Domain generalization via invariant feature representation. In *International Conference on Machine Learning*, pages 10–18. PMLR, 2013.
- [3] Christian Szegedy, Wojciech Zaremba, Ilya Sutskever, Joan Bruna, Dumitru Erhan, Ian Goodfellow, and Rob Fergus. Intriguing properties of neural networks. *arXiv preprint arXiv:1312.6199*, 2013.
- [4] Armen Der Kiureghian and Ove Ditlevsen. Aleatory or epistemic? does it matter? *Structural safety*, 31(2):105–112, 2009.
- [5] Alex Kendall and Yarin Gal. What uncertainties do we need in bayesian deep learning for computer vision? In *Proceedings of the 31st International Conference on Neural Information Processing Systems*, pages 5580–5590, 2017.
- [6] Jasper Snoek, Yaniv Ovadia, Emily Fertig, Balaji Lakshminarayanan, Sebastian Nowozin, D Sculley, Joshua Dillon, Jie Ren, and Zachary Nado. Can you trust your model’s uncertainty? evaluating predictive uncertainty under dataset shift. In *Advances in Neural Information Processing Systems*, pages 13969–13980, 2019.
- [7] Fredrik K Gustafsson, Martin Danelljan, and Thomas B Schon. Evaluating scalable bayesian deep learning methods for robust computer vision. In *Proceedings of the IEEE/CVF Conference on Computer Vision and Pattern Recognition Workshops*, pages 318–319, 2020.
- [8] Radford M Neal et al. Mcmc using hamiltonian dynamics. *Handbook of markov chain monte carlo*, 2(11):2, 2011.
- [9] Radford M Neal. *Bayesian learning for neural networks*, volume 118. Springer Science & Business Media, 2012.
- [10] Geoffrey E Hinton and Drew Van Camp. Keeping the neural networks simple by minimizing the description length of the weights. In *Proceedings of the sixth annual conference on Computational learning theory*, pages 5–13, 1993.
- [11] Balaji Lakshminarayanan, Alexander Pritzel, and Charles Blundell. Simple and scalable predictive uncertainty estimation using deep ensembles. In *Advances in neural information processing systems*, pages 6402–6413, 2017.
- [12] Yeming Wen, Dustin Tran, and Jimmy Ba. Batchensemble: an alternative approach to efficient ensemble and lifelong learning. *arXiv preprint arXiv:2002.06715*, 2020.
- [13] Michael Dusenberry, Ghassen Jerfel, Yeming Wen, Yian Ma, Jasper Snoek, Katherine Heller, Balaji Lakshminarayanan, and Dustin Tran. Efficient and scalable bayesian neural nets with rank-1 factors. In *International conference on machine learning*, pages 2782–2792. PMLR, 2020.
- [14] Durk P Kingma, Tim Salimans, and Max Welling. Variational dropout and the local reparameterization trick. In *Advances in neural information processing systems*, pages 2575–2583, 2015.
- [15] Yarin Gal and Zoubin Ghahramani. Dropout as a bayesian approximation: Representing model uncertainty in deep learning. In *international conference on machine learning*, pages 1050–1059, 2016.
- [16] Guodong Zhang, Shengyang Sun, David Duvenaud, and Roger Grosse. Noisy natural gradient as variational inference. In *International Conference on Machine Learning*, pages 5852–5861. PMLR, 2018.

- [17] Mattias Teye, Hossein Azizpour, and Kevin Smith. Bayesian uncertainty estimation for batch normalized deep networks. In *International Conference on Machine Learning*, pages 4907–4916, 2018.
- [18] Christian Rupprecht, Iro Laina, Robert DiPietro, Maximilian Baust, Federico Tombari, Nassir Navab, and Gregory D Hager. Learning in an uncertain world: Representing ambiguity through multiple hypotheses. In *Proceedings of the IEEE International Conference on Computer Vision*, pages 3591–3600, 2017.
- [19] Janis Postels, Francesco Ferroni, Huseyin Coskun, Nassir Navab, and Federico Tombari. Sampling-free epistemic uncertainty estimation using approximated variance propagation. In *Proceedings of the IEEE International Conference on Computer Vision*, pages 2931–2940, 2019.
- [20] Manuel Haußmann, Fred A Hamprecht, and Melih Kandemir. Sampling-free variational inference of bayesian neural networks by variance backpropagation. In *Uncertainty in Artificial Intelligence*, pages 563–573. PMLR, 2020.
- [21] Antonio Loquercio, Mattia Segù, and Davide Scaramuzza. A general framework for uncertainty estimation in deep learning. *IEEE Robotics and Automation Letters*, 5(2):3153–3160, 2020.
- [22] Amit Mandelbaum and Daphna Weinshall. Distance-based confidence score for neural network classifiers. *arXiv preprint arXiv:1709.09844*, 2017.
- [23] Joost Van Amersfoort, Lewis Smith, Yee Whye Teh, and Yarin Gal. Uncertainty estimation using a single deep deterministic neural network. In *International Conference on Machine Learning*, pages 9690–9700. PMLR, 2020.
- [24] Jeremiah Zhe Liu, Zi Lin, Shreyas Padhy, Dustin Tran, Tania Bedrax-Weiss, and Balaji Lakshminarayanan. Simple and principled uncertainty estimation with deterministic deep learning via distance awareness. *Conference on Neural Information Processing Systems*, 2020.
- [25] Joost van Amersfoort, Lewis Smith, Andrew Jesson, Oscar Key, and Yarin Gal. Improving deterministic uncertainty estimation in deep learning for classification and regression. *arXiv preprint arXiv:2102.11409*, 2021.
- [26] Jishnu Mukhoti, Andreas Kirsch, Joost van Amersfoort, Philip HS Torr, and Yarin Gal. Deterministic neural networks with appropriate inductive biases capture epistemic and aleatoric uncertainty. *arXiv preprint arXiv:2102.11582*, 2021.
- [27] Mike Wu and Noah Goodman. A simple framework for uncertainty in contrastive learning. *arXiv preprint arXiv:2010.02038*, 2020.
- [28] Janis Postels, Hermann Blum, Yannick Strümler, Cesar Cadena, Roland Siegwart, Luc Van Gool, and Federico Tombari. The hidden uncertainty in a neural networks activations. *arXiv preprint arXiv:2012.03082*, 2020.
- [29] Lynton Ardizzone, Jakob Kruse, Sebastian Wirkert, Daniel Rahner, Eric W Pellegrini, Ralf S Klessen, Lena Maier-Hein, Carsten Rother, and Ullrich Köthe. Analyzing inverse problems with invertible neural networks. *arXiv preprint arXiv:1808.04730*, 2018.
- [30] Eric Nalisnick, Akihiro Matsukawa, Yee Whye Teh, Dilan Gorur, and Balaji Lakshminarayanan. Hybrid models with deep and invertible features. In *International Conference on Machine Learning*, pages 4723–4732. PMLR, 2019.
- [31] Lynton Ardizzone, Radek Mackowiak, Carsten Rother, and Ullrich Köthe. Training normalizing flows with the information bottleneck for competitive generative classification. *Advances in Neural Information Processing Systems*, 33, 2020.
- [32] Jonas Peters, Dominik Janzing, and Bernhard Schölkopf. *Elements of causal inference: foundations and learning algorithms*. The MIT Press, 2017.
- [33] Mattia Segù, Alessio Tonioni, and Federico Tombari. Batch normalization embeddings for deep domain generalization. *arXiv preprint arXiv:2011.12672*, 2020.

- [34] Anton Obukhov, Maxim Rakhuba, Alexander Liniger, Zhiwu Huang, Stamatios Georgoulis, Dengxin Dai, and Luc Van Gool. Spectral tensor train parameterization of deep learning layers. In *International Conference on Artificial Intelligence and Statistics*, pages 3547–3555. PMLR, 2021.
- [35] Ishaan Gulrajani, Faruk Ahmed, Martin Arjovsky, Vincent Dumoulin, and Aaron Courville. Improved training of wasserstein gans. *arXiv preprint arXiv:1704.00028*, 2017.
- [36] Takeru Miyato, Toshiki Kataoka, Masanori Koyama, and Yuichi Yoshida. Spectral normalization for generative adversarial networks. *arXiv preprint arXiv:1802.05957*, 2018.
- [37] Hanie Sedghi, Vineet Gupta, and Philip M Long. The singular values of convolutional layers. *arXiv preprint arXiv:1805.10408*, 2018.
- [38] Sahil Singla and Soheil Feizi. Bounding singular values of convolution layers. *arXiv preprint arXiv:1911.10258*, 2019.
- [39] Mihaela Rosca, Theophane Weber, Arthur Gretton, and Shakir Mohamed. A case for new neural network smoothness constraints. *arXiv preprint arXiv:2012.07969*, 2020.
- [40] Alexander A Alemi, Ian Fischer, and Joshua V Dillon. Uncertainty in the variational information bottleneck. *arXiv preprint arXiv:1807.00906*, 2018.
- [41] Aaron van den Oord, Yazhe Li, and Oriol Vinyals. Representation learning with contrastive predictive coding. *arXiv preprint arXiv:1807.03748*, 2018.
- [42] Ting Chen, Simon Kornblith, Mohammad Norouzi, and Geoffrey Hinton. A simple framework for contrastive learning of visual representations. In *International conference on machine learning*, pages 1597–1607. PMLR, 2020.
- [43] Jörn-Henrik Jacobsen, Arnold Smeulders, and Edouard Oyallon. i-revnet: Deep invertible networks. *arXiv preprint arXiv:1802.07088*, 2018.
- [44] J Behrmann, W Grathwohl, RTQ Chen, D Duvenaud, and JH Jacobsen. Invertible residual networks. arxiv e-prints. *arXiv preprint arXiv:1811.00995*, 2018.
- [45] Eric Nalisnick, Akihiro Matsukawa, Yee Whye Teh, Dilan Gorur, and Balaji Lakshminarayanan. Do deep generative models know what they don’t know? In *International Conference on Learning Representations*, 2018.
- [46] Yann LeCun, Léon Bottou, Yoshua Bengio, and Patrick Haffner. Gradient-based learning applied to document recognition. *Proceedings of the IEEE*, 86(11):2278–2324, 1998.
- [47] Carl Edward Rasmussen. Gaussian processes in machine learning. In *Summer school on machine learning*, pages 63–71. Springer, 2003.
- [48] Michalis Titsias. Variational learning of inducing variables in sparse gaussian processes. In *Artificial intelligence and statistics*, pages 567–574. PMLR, 2009.
- [49] James Hensman, Alexander Matthews, and Zoubin Ghahramani. Scalable variational gaussian process classification. In *Artificial Intelligence and Statistics*, pages 351–360. PMLR, 2015.
- [50] David Burt, Carl Edward Rasmussen, and Mark Van Der Wilk. Rates of convergence for sparse variational gaussian process regression. In *International Conference on Machine Learning*, pages 862–871. PMLR, 2019.
- [51] Mahdi Pakdaman Naeini, Gregory Cooper, and Milos Hauskrecht. Obtaining well calibrated probabilities using bayesian binning. In *Proceedings of the AAAI Conference on Artificial Intelligence*, volume 29, 2015.
- [52] GLENN W BRIER. Verification of forecasts expressed in terms of probability. *Monthly Weather Review*, 78(1):1–3, 1950.
- [53] Miha Vuk and Tomaz Curk. Roc curve, lift chart and calibration plot. *Metodoloski zvezki*, 3(1):89, 2006.

- [54] Yann LeCun. The mnist database of handwritten digits. <http://yann.lecun.com/exdb/mnist/>, 1998.
- [55] Han Xiao, Kashif Rasul, and Roland Vollgraf. Fashion-mnist: a novel image dataset for benchmarking machine learning algorithms. *arXiv preprint arXiv:1708.07747*, 2017.
- [56] Alex Krizhevsky, Vinod Nair, and Geoffrey Hinton. The cifar-10 dataset. *online: http://www.cs.toronto.edu/kriz/cifar.html*, 55:5, 2014.
- [57] Yuval Netzer, Tao Wang, Adam Coates, Alessandro Bissacco, Bo Wu, and Andrew Y Ng. Reading digits in natural images with unsupervised feature learning. *arxiv*, 2011.
- [58] Brenden M Lake, Ruslan Salakhutdinov, and Joshua B Tenenbaum. Human-level concept learning through probabilistic program induction. *Science*, 350(6266):1332–1338, 2015.
- [59] Adam Coates, Andrew Ng, and Honglak Lee. An analysis of single-layer networks in unsupervised feature learning. In *Proceedings of the fourteenth international conference on artificial intelligence and statistics*, pages 215–223. JMLR Workshop and Conference Proceedings, 2011.
- [60] Kaiming He, Xiangyu Zhang, Shaoqing Ren, and Jian Sun. Deep residual learning for image recognition. In *Proceedings of the IEEE conference on computer vision and pattern recognition*, pages 770–778, 2016.
- [61] Alexey Dosovitskiy, German Ros, Felipe Codevilla, Antonio Lopez, and Vladlen Koltun. CARLA: An open urban driving simulator. In *Proceedings of the 1st Annual Conference on Robot Learning*, pages 1–16, 2017.
- [62] Marius Cordts, Mohamed Omran, Sebastian Ramos, Timo Rehfeld, Markus Enzweiler, Rodrigo Benenson, Uwe Franke, Stefan Roth, and Bernt Schiele. The cityscapes dataset for semantic urban scene understanding. In *Proc. of the IEEE Conference on Computer Vision and Pattern Recognition (CVPR)*, 2016.
- [63] Fisher Yu and Vladlen Koltun. Multi-scale context aggregation by dilated convolutions. In *International Conference on Learning Representations (ICLR)*, 2016.
- [64] Fisher Yu, Vladlen Koltun, and Thomas Funkhouser. Dilated residual networks. In *Computer Vision and Pattern Recognition (CVPR)*, 2017.
- [65] Hermann Blum, Paul-Edouard Sarlin, Juan Nieto, Roland Siegwart, and Cesar Cadena. The fishyscapes benchmark: Measuring blind spots in semantic segmentation. *arXiv preprint arXiv:1904.03215*, 2019.
- [66] Jean Daunizeau. Semi-analytical approximations to statistical moments of sigmoid and softmax mappings of normal variables. *arXiv preprint arXiv:1703.00091*, 2017.
- [67] Yarin Gal, Riashat Islam, and Zoubin Ghahramani. Deep bayesian active learning with image data. In *Proceedings of the 34th International Conference on Machine Learning-Volume 70*, pages 1183–1192. JMLR. org, 2017.